Fault-Free Integrity Analysis of Mega-Constellation-Augmented GNSS

Danielle Racelis, *Virginia Tech, Blacksburg, VA*
Boris Pervan, *Illinois Institute of Technology, Chicago, IL*
Mathieu Joerger, *Virginia Tech, Blacksburg, VA*

ABSTRACT

In this paper, we evaluate the potential of mega-constellation-augmented GNSS (GNSS-MC) to provide fault-free high-integrity positioning in both open sky and urban areas. We derive a method to integrate dual-frequency carrier-phase ranging measurements from GNSS at medium Earth orbit (MEO), and mega-constellations at low Earth orbit (LEO) to achieve global carrier-phase positioning. From the perspective of users on earth, LEO satellites are moving much faster than GNSS at MEO. The large angular variations generated by these fast-moving LEO satellites are exploited for rapid estimation of floating valued cycle ambiguities. The addition of mega-constellations to GNSS also improves the spatial diversity of ranging sources which enables improved navigation performance in areas where visible GNSS satellites are too few to obtain a position fix, such as in dense cities and urban canyons. This research helps identify the scope of applications potentially enabled by leveraging communication mega-constellations in safety-critical land navigation applications.

1. INTRODUCTION

The accuracy, integrity, continuity, and availability of GNSS-derived position estimates depend on (1) the number of satellites in view, their distribution in the sky, and how that distribution changes over time, and (2) the characteristics of range measurement errors. GPS was designed for open sky scenarios where users who have a clear view of the sky will see the minimum required number of satellites, but it is limited in sky-obstructed areas such as urban canyons for users on land. Also, GPS was designed to be used with code phase ranging measurements, which can be measured with tracking accuracy no better than meter-level.

Carrier phase positioning can achieve centimeter-level positioning errors [1]. The carrier phase of a GNSS signal can be tracked to a precision of 0.05 cycles (~1 cm), but these signals were not intended to be used as ranging measurements, and have inherent cycle ambiguities. The carrier phase cycle ambiguities can be estimated by observing large angular variations in the line-of-sight vectors between the user and visible satellites. The large amount of time needed for GNSS satellites to achieve significant geometric diversity results in long initialization times, and precludes its use in real time applications.

Private companies such as SpaceX, OneWeb, and Boeing are planning to launch mega-constellations composed of hundreds, if not thousands of satellites at low Earth orbit (LEO) with the intention of providing internet worldwide. If the data's carrier signal can be tracked, then the additional ranging sources provided by these mega-constellations present opportunities for improved navigation performance in areas where GNSS satellites are partially obstructed. In addition, from the perspective of users near the surface of the Earth, mega-constellation satellites at LEO move much faster than GNSS satellites at medium Earth Orbit (MEO), and angular variations quickly become substantial for LEO satellites. Therefore, combining measurements from GNSS satellites and LEO mega-constellations makes quick and unambiguous centimeter-level carrier phase positioning possible.

The use of LEO satellites for improved navigation performance is not unexplored. The underlying concept of using spacecraft motion to resolve cycle ambiguities is equivalent to the principle of Doppler positioning used in Transit, the first operational satellite radio-navigation system, whose constellation was also comprised of LEO satellites. Using Transit, the position of stationary receivers could be determined with better than 70 meters of accuracy [2]. The most compelling proof of concept for carrier phase positioning without the stationary user restriction was realized in the late 1990's by Rabinowitz et al [3], with the development of a receiver capable of tracking carrier-phase measurements from GPS and from GlobalStar (another LEO telecommunications constellation). Using satellite motion from fast moving GlobalStar satellites, precise cycle ambiguity resolution and positioning with respect to a nearby reference station was achieved. In [4], the augmentation of GPS with LEO Iridium satellite signals provided signal redundancy and enabled fault-detection using carrier phase Receiver Autonomous Integrity Monitoring (RAIM). Another implementation can

be found in [5] where LEO satellite signals were used to limit the drift of inertial sensors in GPS-denied areas. More recent work in [6] examined the major components that could allow soon to be deployed mega-constellations to act as navigation satellites if they hosted a dedicated payload.

This research focuses on safety-critical navigation applications where integrity is of primary concern. Integrity risk is the probability of undetected faults causing unacceptably large positioning errors. Can mega-constellations, when combined with GNSS, contribute to achieving safety-critical integrity risk requirements? Can they do so in urban areas where low-elevation satellite signals are blocked?

In response, in this work, we quantify the fault-free integrity performance of mega-constellation-augmented GNSS (GNSS-MC) in both open sky and urban environments. This preliminary analysis aims at quantifying the global horizontal positioning performance that can be achieved, based on nominal measurement error models and assumptions that would allow such a multi-constellation system to be leveraged for safety-critical land navigation.

In the second section, we describe a notional system architecture for the combined constellation. Since mega-constellations are primarily intended for communication, assumptions are made regarding the space, ground, and user segments that would allow these LEO satellites to be used for navigation. We consider a candidate architecture where LEO orbit and clock determination is done through a dedicated network of ground stations. The rest of the second section deals with measurement error models over time for the combined system. Signals from fast-moving LEO satellites cross wide sections of the atmosphere within a few minutes, which makes modeling of time-correlated ranging errors due to the troposphere challenging. Additionally, addressing ionospheric anomalies in safety-critical applications is exacting [7, 8]. In this work, we assume dual-frequency LEO carrier measurements, which are combined to eliminate the impact of ionospheric errors. The time-correlated errors due to ephemeris orbit and clock, tropospheric delay, and multipath are modeled as first-order Gauss-Markov processes with bounded variances, and unknown but bounded autocorrelation functions [9]. The remaining errors due to receiver noise are modeled conservatively over time [10].

The third section describes the batch measurement equation, weighted least squares algorithm, implementation of the autocorrelation bounding process, and the protection level (PL) equation. The PL defines a probabilistic bound on positioning error. The PL is set so that the risk of the positioning error exceeding the PL is smaller than a predefined integrity risk requirement. Ionosphere-free GNSS code and carrier measurements, and mega-constellation carrier measurements are processed in a batch to simultaneously estimate three-dimensional position, receiver clock biases (one per constellation when constellations are not synchronized), and cycle ambiguities.

In the fourth section, the horizontal positioning performance of the combined constellation is evaluated. We first analyze the positioning error sensitivity at an example location to elevation mask, batch period, measurement sampling rate, and ephemeris error standard deviation for three configurations: GNSS only, GNSS-OneWeb, and GNSS-Boeing. This local sensitivity analysis quantifies the improvement brought about by GNSS-MC over GNSS alone. Finally, we carry out a worldwide fault-free availability analysis for the combined constellation system when used in open sky versus urban canyon environments, and evaluate the capability of mega-constellations to be used for safe navigation. This fault-free analysis is only the first step to a complete integrity analysis. Future work includes extending the analysis to incorporate fault hypotheses, and evaluating the impact of undetected satellite faults on integrity risk.

2. GNSS-MEGA-CONSTELLATION SYSTEM OVERVIEW, AND MEASUREMENT ERROR MODELS

This paper considers two example GNSS-MC system designs: GNSS-OneWeb and GNSS-Boeing. The assumptions on the space, control, and user segments of the combined systems are discussed first. There are many configurations possible, and the framework described in this section is an example. The rest of this section is devoted to the discussion of measurement equations and error models. *Snapshot* error models for GNSS are well established, but error models *over time* for GNSS and for LEO are not as well understood. Special care has been taken to modify these error models to be applicable for LEO satellite signals.

2.1. Envisioned GNSS-Mega-Constellation System Overview

We assume a dedicated network of ground stations similar to GNSS that would monitor the LEO spacecraft and make the satellite position and time synchronization information available to users. We assume that there are no inter-satellites links.

2.1.1 Envisioned Space Segment

The impending OneWeb satellite constellation aims to provide global satellite Internet broadband services everywhere on Earth by 2027 [11]. In this work, we assume the number of OneWeb satellites is 720 [12]. OneWeb's 720-satellite constellation utilizes a near-polar Walker Star configuration as shown in Figure 1. The constellation design allows satellite coverage at all latitudes at all times. OneWeb's satellites will communicate via the Ka- and Ku- spectrum bands [12]. The first six OneWeb satellites were successfully launched in February 2019 [13].

Boeing plans to deploy a 2956-satellite constellation in low Earth orbit, and filed for spectrum allocation with the Federal Communications Commission (FCC) in 2016 [14]. Boeing intends to use V- and C-bands [15]. In this work, we assume the satellite configuration for Boeing depicted in Figure 2. In this figure, the three colors distinguish three different constellation configurations. Boeing's 2956-satellite constellation has both near-polar and inclined orbits.

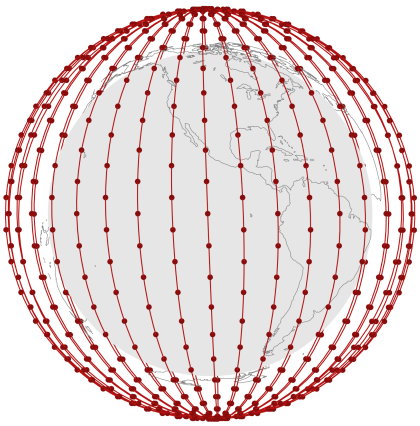

Figure 1: OneWeb Constellation. The 720-satellite OneWeb constellation used in the simulations has 18 orbital planes inclined at 87.9° at 1200 km altitude. This configuration is based on information found in [12].

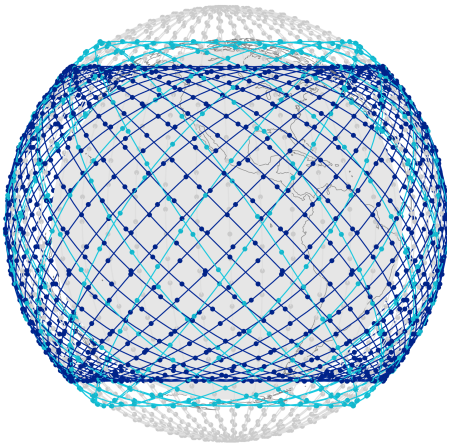

Figure 2: Boeing Constellation. The 2956-satellite Boeing constellation used in the simulations has 1225 satellites in 35 planes inclined at 45°, and 576 satellites in 18 planes inclined at 55° at 1200 km altitude. Additionally, there are 1155 satellites in 21 more orbital planes inclined at 88° at 1000 km altitude. This configuration is based on information found in [15].

Unless differential corrections are available, dual-frequency signals are essential to mitigate the impact of ionospheric delay. We assume dual-frequency carrier signals from mega-constellation satellites. Both OneWeb and Boeing have indicated capability of providing dual-frequency signals [16, 15].

A satellite at low Earth orbit services a smaller geographic region on Earth than a satellite at medium Earth orbit, referred to as a smaller satellite footprint. Satellite footprints depend on many factors including Earth terrain, and antenna gain patterns. Ideally, constellation orbits are designed so that the footprint of each satellite overlap, and the constellation provides continuous global coverage at all times. In this preliminary work, we assume that there is no limit on the LEO spacecraft footprint, and that measurements can be received from all visible satellites.

2.1.2 Envisioned Control Segment

A dedicated ground control segment is envisioned to perform orbit and clock determination for the LEO mega-constellations. The ground monitoring stations can be collocated with data monitoring stations needed for the communications function of the satellite. OneWeb has plans for more than fifty ground stations globally for communication [12, 17]. Mega-constellation LEO satellite orbit and clock offsets are estimated and monitored by a dedicated network of ground stations, uploaded to the satellites, and broadcast to users. We assume that the mega-constellations are time-synchronized with GPS. The clocks aboard LEO communication spacecraft are not expected to have the same standard as those aboard GNSS satellites. However high throughput data links can be established between the satellites and the control segment [16]. Higher data rates and more frequent updates to the broadcast message could potentially compensate for the not-so-accurate clocks aboard the LEO satellites [6].

2.1.3 Envisioned User Segment

We assume that the user is equipped with a dual-frequency receiver capable of processing measurements from GNSS and mega-constellations. The dual frequency capability is an important simplifying assumption that eliminates the impact of ionospheric errors.

2.2. Nominal Measurement Error Models

Under nominal fault-free conditions, the linearized ionosphere-error-free carrier phase and code measurement equations for satellite i at time k respectively are

$$\begin{aligned} {}^{i}\phi_k &= -{}^{i}\mathbf{e}_k^{\mathrm{T}}\mathbf{x}_k + \tau_k + {}^{i}\eta + {}^{i}\mathscr{E}_{E,k} + {}^{i}\mathscr{E}_{T,k} + {}^{i}\mathscr{E}_{M,\phi,k} + {}^{i}\mathscr{E}_{R,\phi,k} \\ {}^{i}\rho_k &= -{}^{i}\mathbf{e}_k^{\mathrm{T}}\mathbf{x}_k + \tau_k + {}^{i}\mathscr{E}_{E,k} + {}^{i}\mathscr{E}_{T,k} + {}^{i}\mathscr{E}_{M,\rho,k} + {}^{i}\mathscr{E}_{R,\rho,k} \end{aligned} \tag{1}$$

where

${}^{i}\phi_k$	is the carrier phase measurement for satellite i,
${}^{i}\rho_k$	is the code phase measurement for satellite i,
${}^{i}\mathbf{e}_k$	is the 3×1 line-of-sight vector from the satellite to the user in North-East-Down (NED),
$\mathbf{x}_k$	is the user position in NED,
τ_k	is the receiver clock offset,
${}^{i}\eta$	is the carrier phase cycle ambiguity,
	(there is no subscript k because it is constant over time)
${}^{i}\mathscr{E}_{E,k}$	is the satellite clock and orbit ephemeris error,
${}^{i}\mathscr{E}_{T,k}$	is the residual tropospheric error,
${}^{i}\mathscr{E}_{M,k}$	is the multipath error, and
${}^{i}\mathscr{E}_{R,k}$	is the receiver noise error.

GPS and Galileo provide carrier and code phase measurements, while the OneWeb and Boeing LEO constellations provide carrier phase measurements only.

2.2.1 Satellite Orbit and Clock Error

The satellite orbit and clock error is modeled using a first-order Gauss-Markov Process (GMP) with Markov process correlation time constant T_E, and driving noise $\nu_{E,k}$. We will relax this assumption in Section 3.4. It is assumed that there is no correlation between measurements from different satellites [18, 19, 20], and that the clocks on the LEO satellites are synchronized with GPS. The error due to satellite orbit and clock for satellite i at time k is

$${}^{i}\mathscr{E}_{E,k} = e^{-T_s/T_E}\,{}^{i}\mathscr{E}_{E,k-1} + \nu_{E,k} \qquad , \qquad \nu_{E,k} \sim N\left(0, \sigma_E^2\left(1 - e^{-2T_s/T_E}\right)\right) \tag{2}$$

where $T_s = t_k - t_{k-1}$ (sampling interval), and σ_E is the GMP standard deviation. The GMP standard deviation and correlation time constant for ground vehicle applications are given in Table 1 for GNSS [21, 10]. The LEO satellite clock and orbit ephemeris are assumed to be updated once per orbit for a LEO orbital period of 100 minutes. This assumption coupled with a 50% increase in the GMP standard deviation results in the error parameters found in Table 1. These values for the LEO orbit and clock error have not been verified, but are recognized as a good starting point based on discussions in [6].

2.2.2 Residual Tropospheric Error

Most of the error caused by tropospheric delay is removed using a model of the troposphere. The residual tropospheric error is treated as a first-order GMP. The error variation caused by signals traveling through the troposphere at different angles is accounted for by using the mapping function described in [10]. The resulting error contribution for satellite i at time k is given by

$${}^{i}\mathscr{E}_{T,k} = {}^{i}c_{T,k}\,{}^{i}\zeta_{T,k} \tag{3}$$

where the elevation-dependent tropospheric correction mapping function [10] is

$${}^{i}c_{T,k} = \frac{1.001}{\sqrt{0.002001 + \left(\sin({}^{i}\theta_k[\mathrm{rad}])\right)^2}} \tag{4}$$

for satellite elevation angles ${}^{i}\theta_k \geq 4°$. The residual tropospheric error at zenith is modeled as

$$ {}^{i}\zeta_{T,k} = e^{-T_s/T_T}\ {}^{i}\zeta_{T,k-1} + \nu_{T,k} \qquad , \qquad \nu_{T,k} \sim N\left(0, \sigma_T^2\left(1 - e^{-2T_s/T_T}\right)\right) \ . \tag{5} $$

The GMP correlation time constant and standard deviation are retrieved from [22] and are given in Table 1, where 0.12 m is the tropospheric vertical error standard deviation given in A.4.2.5 of [22]. Since the tropospheric model characterizes the airmass encountered by the signal, the model is the same for GNSS and mega-constellations. The difference in satellite motion is captured in the elevation-dependent mapping coefficient, Eq. (4).

2.2.3 Multipath Error

In order to account for the time-correlation caused by unwanted signal reflections reaching the receiver antenna, the multipath error is modeled as a first-order GMP, multiplied by the elevation-dependent mapping function given in [22]. The multipath error contribution for satellite i at time k is given by

$$ \begin{aligned} {}^{i}\mathscr{E}_{M,\phi,k} &= {}^{i}c_{M,k}\,{}^{i}\zeta_{M,\phi,k} \\ {}^{i}\mathscr{E}_{M,\rho,k} &= {}^{i}c_{M,k}\,{}^{i}\zeta_{M,\rho,k} \end{aligned} \tag{6} $$

where the elevation-dependent multipath mapping function is

$$ {}^{i}c_{M,k} = (10)\, c_{IF}\left(0.13 + 0.53\, e^{\left(-{}^{i}\theta_k\,[\mathrm{deg}]/10\right)}\right). \tag{7} $$

The factor 10 comes from using raw unsmoothed code measurements which can be up to 10 times noisier than carrier-smoothed code measurements [10]. The ionosphere-free measurement combination multiplier, c_{IF} is computed with L1 and L5 and given by the equation

$$ c_{IF} = \sqrt{\frac{f_{L1}^4 + f_{L5}^4}{\left(f_{L1}^2 - f_{L5}^2\right)^2}} \tag{8} $$

where f_{L1} and f_{L5} are the frequencies for L1 and L5 respectively. The use of equivalent c_{IF} values for all constellations is a simplifying assumption that can be refined in future work. The GMP term in Eq. (6) for carrier and code measurements are

$$ \begin{aligned} {}^{i}\zeta_{M,\phi,k} &= e^{-T_s/T_M}\ {}^{i}\zeta_{M,\phi,k-1} + \nu_{M,\phi,k} \qquad , \qquad \nu_{M,\phi,k} \sim N\left(0, \sigma_{M,\phi}^2\left(1 - e^{-2T_s/T_M}\right)\right) \\ {}^{i}\zeta_{M,\rho,k} &= e^{-T_s/T_M}\ {}^{i}\zeta_{M,\rho,k-1} + \nu_{M,\rho,k} \qquad , \qquad \nu_{M,\rho,k} \sim N\left(0, \sigma_{M,\rho}^2\left(1 - e^{-2T_s/T_M}\right)\right). \end{aligned} \tag{9} $$

GNSS multipath error has been modeled for automotive applications in [23], where values for the correlation time constant and pseudorange bounding standard deviation can be used as reference. These values were taken into account to get the parameters for GNSS listed in Table 1, where the order of magnitude difference in multipath error between code and carrier is accounted for.. We assume a similarly derived GMP standard deviation for the LEO constellations, but deriving the time constant is trickier. LEO satellites move faster, so the correlation time constant needs to be appropriately scaled down. For this, we use the ratio of angular velocities between GNSS and mega-constellations relative to a user on Earth. We use as reference the angular velocity ratio derived in [24] between GPS and a constellation of LEO satellites called Iridium, which was evaluated every 30s over a 3-day period to compute for the average ratio of 30. Later we will find that the scaled LEO time constant can be much smaller than the batch measurement sampling rate in our example implementation. This implies that multipath error does not appear correlated in time for LEO carrier phase measurements as sampled in our positioning algorithm.

2.2.4 Receiver Noise Error

Receiver noise is modeled as Gaussian white noise with elevation-dependent standard deviation, and is computed as

$$ \begin{aligned} {}^{i}\mathscr{E}_{R,\phi,k} &= {}^{i}\nu_{R,\phi,k} \qquad , \qquad {}^{i}\nu_{R,\phi,k} \sim N(0, {}^{i}\sigma_{R,\phi}^2) \\ {}^{i}\mathscr{E}_{R,\rho,k} &= {}^{i}\nu_{R,\rho,k} \qquad , \qquad {}^{i}\nu_{R,\rho,k} \sim N(0, {}^{i}\sigma_{R,\rho}^2) \end{aligned} \ . \tag{10} $$

Elevation-dependent receiver noise error models are formulated for airborne aircraft using carrier-smoothed code measurements from GNSS in [21]. Error due to raw unsmoothed code can be up to 10 times greater [10]. The effect of receiver noise is assumed to be the same for MEO and LEO measurements. The equations for these prameters are

$$ {}^{i}\sigma_{R,MEO,\rho,k} = (10)\, c_{IF}\left(0.15 + 0.43\, e^{\left(-{}^{i}\theta_k\,[\mathrm{deg}]/6.9\right)}\right) \tag{11} $$

$$ {}^{i}\sigma_{R,MEO/LEO,\phi,k} = \left(\frac{1}{100}\right){}^{i}\sigma_{R,MEO,\rho,k} \tag{12} $$

2.2.5 Summary of Error Parameters

The values allocated for the measurement error parameters for ground vehicle applications are summarized in Table 1 for GNSS (GPS/Galileo) and mega-constellations (OneWeb/Boeing). These error models will have to be further evaluated using experimental data. In particular, data processing is necessary to validate the LEO measurement error models discussed in this section.

Table 1: Summary of GMP Error Model Parameters

GMP	Carrier/Code	GPS/Galileo	OneWeb/Boeing
		Clock and Orbit Ephemeris	
σ_E		1 m	1.5 m
T_E		7200 s	6000 s
		Troposphere	
σ_T		0.12 m	0.12 m
T_T		1800 s	1800 s
		Multipath	
σ_M	ϕ	0.015 m	0.015 m
	ρ	1.5 m	
T_M		158 s	6 s
		Receiver Noise	
σ_R	ϕ	Eq.(12)	Eq.(12)
	ρ	Eq.(11)	

3. GNSS-MEGA-CONSTELLATION POSITIONING ALGORITHM

In this section, we derive a batch weighted least squares algorithm for estimating the user parameters using dual-frequency code and carrier phase measurements from GNSS, and dual-frequency carrier phase measurements from mega-constellations. This algorithm simultaneously estimates the three-dimensional user position and receiver clock offset at every time step, and estimates the floating valued carrier phase cycle ambiguities that remain constant, as long as the carrier is tracked continuously. The process assumes no knowledge about the user's dynamics, but captures the fact that cycle ambiguities remain constant. We assume that there are no unrepaired cycle slips. This batch approach leverages two estimation principles: noise averaging and bias observability by exploiting satellite motion. It can be implemented in practical applications as long as adequate receiver memory is available to store current and past measurements [25]. This method can be implemented sequentially in a sliding window mechanism, and will leverage fault detection algorithms in future work [26, 27, 28].

3.1. Batch Measurement Equation

This section aims at deriving a batch measurement equation of the form:

$$\mathbf{z} = \mathbf{H}\,\mathbf{x} + \mathbf{v} \tag{13}$$

which expresses the linear relationship between the measurements $\mathbf{z}$, and the states $\mathbf{x}$. Vectors are expressed in lowercase boldface characters, and matrices are denoted by uppercase boldface characters. In this equation, $\mathbf{H}$ is the observation matrix, and $\mathbf{v}$ is the measurement noise vector. We start with the linearized measurement equations for ionosphere-error-free carrier and code phase measurements Eq. (1) for satellite i at time k. For convenience in building the matrices for batch processing, the following vectors

are defined

$$\mathbf{u}_k = \begin{bmatrix} \mathbf{x}_k \\ \tau_{\text{GPS},k} \\ \tau_{\text{Gal},k} \end{bmatrix} \tag{14}$$

$${}^i\mathbf{g}_k^{\mathrm{T}} = \begin{bmatrix} -{}^i\mathbf{e}_k^{\mathrm{T}} & 1 & 0 \end{bmatrix} \text{ if satellite } i \text{ is a GPS, OneWeb, or Boeing satellite} \tag{15}$$

$${}^i\mathbf{g}_k^{\mathrm{T}} = \begin{bmatrix} -{}^i\mathbf{e}_k^{\mathrm{T}} & 0 & 1 \end{bmatrix} \text{ if satellite } i \text{ is a Galileo satellite} \tag{16}$$

$${}^i\nu_{\phi,k} = {}^i\mathscr{E}_{E,k} + {}^i\mathscr{E}_{T,k} + {}^i\mathscr{E}_{M,\phi,k} + {}^i\mathscr{E}_{R,\phi,k} \tag{17}$$

$${}^i\nu_{\rho,k} = {}^i\mathscr{E}_{E,k} + {}^i\mathscr{E}_{T,k} + {}^i\mathscr{E}_{M,\rho,k} + {}^i\mathscr{E}_{R,\rho,k} \tag{18}$$

Galileo employs a different time reference from GPS Time, which results in a distinct receiver clock bias $\tau_{\text{Gal,k}}$. In this preliminary analysis, mega-constellations are assumed to be synchronized with GPS, and share the same receiver clock bias $\tau_{\text{GPS},k}$. In future work, this assumption can be relaxed to where each constellation can have their own clock bias, and satellites are time-synchronized only within each constellation.

Consider measurements for both GNSS and LEO satellites from times 1 to q. Measurements from distinct satellites are designated by the left superscript i, which goes from 1 to n, where n is the total number of satellites in view. For clarity of presentation, we consider that measurements for visible satellites are available throughout the batch period. In practice, satellites can rise and set within the batch period, and this occurrence is frequent for low Earth-orbiting (LEO) satellites. Our actual implementation accounts for satellites coming in and out of view. Further details on procedures to account for satellites rising and setting can be found in [29].

We stack measurements over time for satellites i. The resulting geometry matrix, carrier and code measurements, carrier and code measurement noise vectors, and user states are respectively expressed as

$${}^i\mathbf{G} = \begin{bmatrix} {}^i\mathbf{g}_1^{\mathrm{T}} & & \mathbf{0} \\ & \ddots & \\ \mathbf{0} & & {}^i\mathbf{g}_q^{\mathrm{T}} \end{bmatrix} \quad {}^i\boldsymbol{\varphi} = \begin{bmatrix} {}^i\phi_1 \\ \vdots \\ {}^i\phi_q \end{bmatrix} \quad {}^i\boldsymbol{\rho} = \begin{bmatrix} {}^i\rho_1 \\ \vdots \\ {}^i\rho_q \end{bmatrix} \quad {}^i\mathbf{v}_\phi = \begin{bmatrix} {}^i\nu_{\phi,1} \\ \vdots \\ {}^i\nu_{\phi,q} \end{bmatrix} \quad {}^i\mathbf{v}_\rho = \begin{bmatrix} {}^i\nu_{\rho,1} \\ \vdots \\ {}^i\nu_{\rho,q} \end{bmatrix} \quad \mathbf{u} = \begin{bmatrix} \mathbf{u}_1 \\ \vdots \\ \mathbf{u}_q \end{bmatrix}$$

The measurements get stacked with GNSS carrier phase measurements first, followed by LEO carrier phase measurements, then GNSS code measurements. The resulting stack of measurements is

$$\begin{bmatrix} {}^1\boldsymbol{\varphi} \\ {}^2\boldsymbol{\varphi} \\ \vdots \\ {}^n\boldsymbol{\varphi} \\ {}^1\boldsymbol{\rho} \\ {}^2\boldsymbol{\rho} \\ \vdots \\ {}^{n_{GNSS}}\boldsymbol{\rho} \end{bmatrix} = \begin{bmatrix} {}^1\mathbf{G} & \mathbf{1}_{q\times 1} & 0 & & 0 \\ {}^2\mathbf{G} & 0 & \mathbf{1}_{q\times 1} & & 0 \\ \vdots & \vdots & \vdots & \ddots & \vdots \\ {}^n\mathbf{G} & 0 & 0 & & \mathbf{1}_{q\times 1} \\ {}^1\mathbf{G} & 0 & 0 & & 0 \\ {}^2\mathbf{G} & 0 & 0 & & 0 \\ \vdots & \vdots & \vdots & \ddots & \vdots \\ {}^{n_{GNSS}}\mathbf{G} & 0 & 0 & & 0 \end{bmatrix} \begin{bmatrix} \mathbf{u} \\ {}^1\eta \\ {}^2\eta \\ \vdots \\ {}^n\eta \end{bmatrix} + \begin{bmatrix} {}^1\mathbf{v}_\phi \\ {}^2\mathbf{v}_\phi \\ \vdots \\ {}^n\mathbf{v}_\phi \\ {}^1\mathbf{v}_\rho \\ {}^2\mathbf{v}_\rho \\ \vdots \\ {}^{n_{GNSS}}\mathbf{v}_\rho \end{bmatrix} \tag{19}$$

where the left superscript n_{GNSS} distinguishes the number of visible GNSS satellites from the left superscript n indicating the total number of visible satellites (including LEOs). Furthermore, stacking measurements and cycle ambiguity states for satellites $i = 1, ..., n$, we define

$$\boldsymbol{\varphi} = \begin{bmatrix} {}^1\boldsymbol{\varphi} \\ \vdots \\ {}^n\boldsymbol{\varphi} \end{bmatrix} \quad \boldsymbol{\rho} = \begin{bmatrix} {}^1\boldsymbol{\rho} \\ \vdots \\ {}^{n_{GNSS}}\boldsymbol{\rho} \end{bmatrix} \quad \mathbf{G}_\phi = \begin{bmatrix} {}^1\mathbf{G} \\ \vdots \\ {}^n\mathbf{G} \end{bmatrix} \quad \mathbf{G}_\rho = \begin{bmatrix} {}^1\mathbf{G} \\ \vdots \\ {}^{n_{GNSS}}\mathbf{G} \end{bmatrix} \quad \mathbf{H}_N = \begin{bmatrix} \mathbf{1}_{q\times 1} & & \mathbf{0}_{q\times 1} \\ & \ddots & \\ \mathbf{0}_{q\times 1} & & \mathbf{1}_{q\times 1} \end{bmatrix}$$

$$\boldsymbol{\eta} = \begin{bmatrix} {}^1\eta \\ \vdots \\ {}^n\eta \end{bmatrix} \quad \mathbf{v}_\phi = \begin{bmatrix} {}^1\mathbf{v}_\phi \\ \vdots \\ {}^n\mathbf{v}_\phi \end{bmatrix} \quad \mathbf{v}_\rho = \begin{bmatrix} {}^1\mathbf{v}_\rho \\ \vdots \\ {}^{n_{GNSS}}\mathbf{v}_\rho \end{bmatrix} .$$

Finally, we get the batch measurement equation in the form of Eq. (13)

$$\begin{bmatrix} \boldsymbol{\varphi} \\ \boldsymbol{\rho} \end{bmatrix} = \begin{bmatrix} \mathbf{G}_\phi & \mathbf{H}_N \\ \mathbf{G}_\rho & \mathbf{0} \end{bmatrix} \begin{bmatrix} \mathbf{u} \\ \boldsymbol{\eta} \end{bmatrix} + \begin{bmatrix} \mathbf{v}_\phi \\ \mathbf{v}_\rho \end{bmatrix} \tag{20}$$

where

$$\mathbf{z} = \begin{bmatrix} \boldsymbol{\varphi} \\ \boldsymbol{\rho} \end{bmatrix} \qquad \mathbf{H} = \begin{bmatrix} \mathbf{G}_\phi & \mathbf{H}_N \\ \mathbf{G}_\rho & \mathbf{0} \end{bmatrix} \qquad \mathbf{x} = \begin{bmatrix} \mathbf{u} \\ \boldsymbol{\eta} \end{bmatrix} \qquad \mathbf{v} = \begin{bmatrix} \mathbf{v}_\phi \\ \mathbf{v}_\rho \end{bmatrix}.$$

3.2. Batch Measurement Error Covariance Matrix Accounting for Measurement Error Correlation

Recall from Section 2.2 that the measurement error models for the satellite ephemeris, tropospheric, and multipath error are correlated in time for each satellite. We express the batch measurement error covariance matrix as

$$\mathbf{V} = E\left\{ \begin{bmatrix} \mathbf{v}_\phi \\ \mathbf{v}_\rho \end{bmatrix} \begin{bmatrix} \mathbf{v}_\phi^{\mathrm{T}} & \mathbf{v}_\rho^{\mathrm{T}} \end{bmatrix} \right\} = \begin{bmatrix} \mathbf{V}_{\phi\phi} & \mathbf{V}_{\phi\rho} \\ \mathbf{V}_{\rho\phi} & \mathbf{V}_{\rho\rho} \end{bmatrix}. \tag{21}$$

The satellite ephemeris and residual tropospheric error affects code and carrier phase measurements equally. In contrast, multipath and receiver noise error have different effects on code and carrier phase measurements. We can express $\mathbf{V}$ as

$$\mathbf{V} = \begin{bmatrix} \mathbf{V}_E + \mathbf{V}_T & \mathbf{V}_E + \mathbf{V}_T \\ \mathbf{V}_E + \mathbf{V}_T & \mathbf{V}_E + \mathbf{V}_T \end{bmatrix} + \begin{bmatrix} \mathbf{V}_{\phi\phi,M} + \mathbf{V}_{\phi\phi,R} & \mathbf{0} \\ \mathbf{0} & \mathbf{V}_{\rho\rho,M} + \mathbf{V}_{\rho\rho,R} \end{bmatrix} \tag{22}$$

where

$\mathbf{V}_E$ is the ephemeris error covariance,
$\mathbf{V}_T$ is the residual tropospheric error covariance,
$\mathbf{V}_M$ is the multipath error covariance, and
$\mathbf{V}_R$ is the receiver noise error covariance.

The derivation for the time-correlated error terms in these covariance matrices is in the Appendix.

3.3. Batch Estimator

The weighted least squares estimate $\hat{\mathbf{x}}$ that minimizes the sum of squares of the weighted observation errors is given as

$$\hat{\mathbf{x}} = \mathbf{S}\mathbf{z} \tag{23}$$

where

$$\mathbf{S} = \left(\mathbf{H}^{\mathrm{T}}\mathbf{V}^{-1}\mathbf{H}\right)^{-1}\mathbf{H}^{\mathrm{T}}\mathbf{V}^{-1} \tag{24}$$

with covariance matrix

$$\mathbf{P} = \left(\mathbf{H}^{\mathrm{T}}\mathbf{V}^{-1}\mathbf{H}\right)^{-1}. \tag{25}$$

3.4. Positioning Error Variance Bounding Method to Account for Error Time Correlation Uncertainty

In order to account for the uncertainty in the measurement error model GMP time constants, we use a method developed in [9] that allows us to determine an overbound on the unknown time constant. It is shown in [30], that using the maximum time constant will not always produce an upperbound on the estimate error. Experimental data show that measurement time correlation due to ephemeris, multipath, and troposphere errors do not behave like the first order GMP (FOGMP) models assumed in Section 2.2 [31, 32, 33]. To address this issue, Langel derived a method in [9] that makes no assumption on the error autocorrelation function other than it can be bounded by a pair of FOGMP autocorrelation functions. Thus, in this work, we assume a pair of GMP autocorrelation functions using $T_{\max}$ and $T_{\min}$ can be used to bound the unknown autocorrelation, which does not have to be a FOGMP.

For ground vehicle applications, we are primarily concerned with the 2×2 current time horizontal (in the North and East directions) position estimate covariance matrix $\mathbf{P}_{\mathrm{NE},q}$. This 2D covariance matrix, can be represented as a covariance ellipse, with maximum horizontal positioning uncertainty equal to the maximum eigenvalue of $\mathbf{P}_{\mathrm{NE},q}$. We are interested in upperbounding the estimate variance for the horizontal position. We first define the estimator vector for the horizontal position

$$\mathbf{s}_H = \left[\boldsymbol{\alpha}_H^{\mathrm{T}} \mathbf{S}\right]_{1\times N} \tag{26}$$

where $\mathbf{S}$ uses the maximum time constants for the error models used in $\mathbf{V}$. The first term $\boldsymbol{\alpha}_H^{\mathrm{T}}$ is a row vector of length equal to the number of states, composed of zeros except for the elements corresponding to the North and East position states at current time. To account for the worst case impact in the horizontal position variance, the eigenvector corresponding to the maximum eigenvalue of $\mathbf{P}_{\mathrm{NE},q}$ is used for these non-zero elements. We rewrite the estimation error variance for the horizontal position using an equivalent expression [9]

$$\sigma_H^2 = \sum_{i=1}^{N}\sum_{j=1}^{N} [\mathbf{M} \circ \mathbf{V}]_{i,j} \tag{27}$$

$$\tag{28}$$

where $\mathbf{M} = \left[\mathbf{s}_H^{\mathrm{T}} \mathbf{s}_H\right]_{N\times N}$, and the symbol "$\circ$" represents element-wise matrix multiplication. In the following paragraphs, we derive a practical way to implement the method in [9]. Following the method in [9], we add up the variance contributions in the worst-conspiring manner using the following equations.

$$\sigma_+^2 = \sum_{i=1}^{N}\sum_{j=1}^{N} [\mathbf{M}_+ \circ \mathbf{V}(T_{max})]_{i,j} \qquad \text{where} \qquad [\mathbf{M}_+]_{i,j} = \begin{cases} \left[\mathbf{s}_H^{\mathrm{T}} \mathbf{s}_H\right]_{i,j} \text{ if } \left[\mathbf{s}_H^{\mathrm{T}} \mathbf{s}_H\right]_{i,j} \geq 0 \\ 0 \qquad \text{otherwise} \end{cases} \tag{29}$$

$$\sigma_-^2 = \sum_{i=1}^{N}\sum_{j=1}^{N} [\mathbf{M}_- \circ \mathbf{V}(T_{min})]_{i,j} \qquad \text{where} \qquad [\mathbf{M}_-]_{i,j} = \begin{cases} \left[\mathbf{s}_H^{\mathrm{T}} \mathbf{s}_H\right]_{i,j} \text{ if } \left[\mathbf{s}_H^{\mathrm{T}} \mathbf{s}_H\right]_{i,j} < 0 \\ 0 \qquad \text{otherwise} \end{cases} \tag{30}$$

$$\sigma_{H,b}^2 = \sigma_+^2 + \sigma_-^2 \geq \sigma_H^2 \tag{31}$$

where $\sigma_{H,b}^2$ bounds the variance produced by simply using the maximum time constants in $\mathbf{V}$. As a preliminary analysis, the range of GMP time constants $[T_{min}, T_{max}]$ is taken to be $[0.8T_\varepsilon, 1.2T_\varepsilon]$, where T_ε is the GMP time constant specified for each measurement error model in Section 2.2. The subscript ε denotes E, T, M for ephemeris, troposphere, and multipath errors respectively. In future work, we will consider more realistic ranges of values that have recently been published in [31].

3.5. Fault-Free Protection Level Derivation

In this fault-free availability analysis, the GNSS-MC system is required to meet an example integrity risk requirement of $I_{\mathrm{req}} = 10^{-5}$. This means that the probability that the horizontal positioning error exceeds the horizontal protection level (HPL) is less than or equal to 10^{-5} or $P(|\mathscr{E}_H| > \mathrm{HPL}, H_0) \leq I_{\mathrm{req}}$, where H_0 is the fault-free hypothesis. For this integrity risk requirement, the fault-free horizontal protection level (HPL_0) is computed as

$$\mathrm{HPL}_0 = Q^{-1}\left(\frac{I_{\mathrm{req}}}{2}\right)\sigma_{H,b} \tag{32}$$

where $\sigma_{H,b}$ is given by Eq. (31). The Q^{-1}-function is the inverse tail distribution function of the standard normal distribution. In other words, $I_{\mathrm{req}}/2$ is the probability that a standard normal variable takes a value larger than $Q^{-1}\left(I_{\mathrm{req}}/2\right)$.

Significant work and testing goes into the definition of a horizontal alert limit (HAL), and it is application-specific (e.g. different between aircraft and automotive applications). In this preliminary work, we assume a HAL of 1.5 m, and the fault-free availability criterion is $\mathrm{HPL}_0 < \mathrm{HAL}$. This example value for HAL will be refined in future work for specific applications.

4. PERFORMANCE ANALYSIS

We assess the horizontal positioning integrity performance of three configurations: GNSS only, GNSS-OneWeb, and GNSS-Boeing. A sensitivity analysis is performed to evaluate the effects of varying elevation mask, batch period, measurement sampling rate, and orbit ephemeris error.

4.1. Covariance Analysis Implementation

In this section, we describe the implementation of the covariance analysis. We consider a nominal configuration that uses OneWeb-augmented GNSS. A 40-degree elevation mask is applied as a simplified model for sky obstruction due to buildings and trees in urban environments. A 10-minute batch is performed. Within the batch period, measurements are sampled for the estimator every 1 minute. We simulate such batches repeatedly at regular 1 minute intervals over 24 hours at a reference location in Tucson, Arizona (32.2369278°N, 110.951933°W, 752m altitude). The measurement sampling rate and batch period are chosen so that we are taking measurements frequent enough to average out noise, and the batch period is long enough to take advantage of satellite motion. Based on each 10-minute batch, the final position covariance is stored for analysis. Figure 3's top plot shows the positioning error standard deviations in the North, East, and Down directions for the entire day.

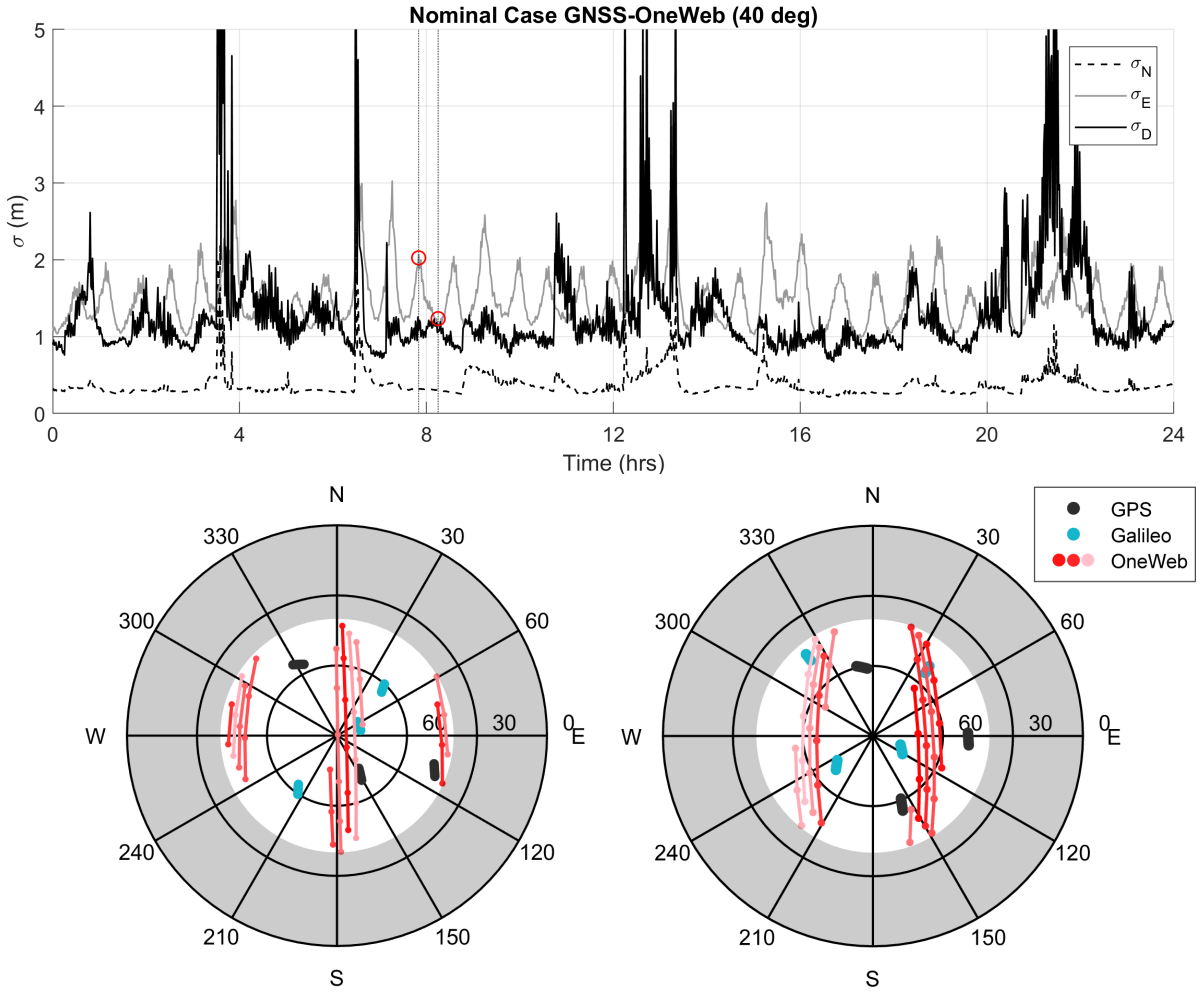

Figure 3: Positioning Performance for OneWeb-augmented GNSS Using a 40° Elevation Mask in Tucson, Arizona. The top plot shows the positioning error standard deviations in the North, East, and Down directions during the 24-hour simulation. The two azimuth-elevation (AzEl) plots are for two time instances indicated by red circles and vertical dotted lines on the top plot. The left AzEl plot is for the batch at 7.83-hr where σ_E reaches a local peak. The right AzEl plot is for the batch at 8.25-hr where σ_E is at a relative minimum.

The OneWeb constellation uses near polar orbits, which means that over the 10-minute batch period while the GNSS satellites appear static for a user on Earth, OneWeb satellites cross the entire sky in the North-South direction. As a result, the uncertainty in the North direction is lowest. At a high elevation mask of 40 degrees, the positioning error in the Down direction has the largest peaks. These peaks correspond to times when there are at most two GPS satellites or at most two Galileo satellites (see bottom plot of Figure 5). The positioning error in the East direction is bounded between 1 and ~3 meters. This peculiar behavior of σ_E can be explained with the help of the two azimuth-elevation (AzEl) plots on the bottom of Figure 3. The fluctuation of σ_E is due to the fact that the Earth rotates with respect to Earth-centered inertial (ECI) frame, while the LEO satellites move in quasi-stationary

orbital planes. Thus, the reference location on Earth moves with respect to the near-polar OneWeb orbits. Peaks in σ_E occur when the user is directly below an orbital plane where North-South spacecraft motion is substantial, but East-West spacecraft motion is small. The valleys in σ_E occur when the user is in between two orbital planes where the satellites are distributed on either side, and East-West spacecraft motion is more substantial. Reference [24] gives a detailed explanation of a similar observation for navigation performance using GPS and Iridium (a 66-satellite LEO communications constellation with near polar orbits). There is no difference in positioning performance at the seam of the constellation, between 16 and 18 hours.

4.2. Performance Sensitivity Analysis

The objective of this section is to identify sensitive parameters that are key to leveraging future communication mega-constellations in safety-critical navigation applications. To achieve this, we do a detailed analysis at a single user location.

4.2.1 Performance Sensitivity to Elevation Mask

We are quantifying the navigation performance of the combined system in both open sky and urban canyon environments. In urban canyon environments, views of the sky can be partially obscured by tall buildings, bridges, trees, and other obstacles.To analyze the impact of sky obstructions, we implement a batch covariance analysis for a range of elevation masks at Tucson, Arizona. At each elevation mask, 10-minute batches are simulated every minute over 24 hours. In Figure 4, the maximum $\sigma_{H,b}$ value over the 24-hour simulation period is plotted for elevation masks ranging from 5° to 60° using GNSS only, GNSS-OneWeb, and GNSS-Boeing. The bottom plot of Figure 4 shows the minimum number of visible satellites for the 24-hour simulation period at each elevation mask.

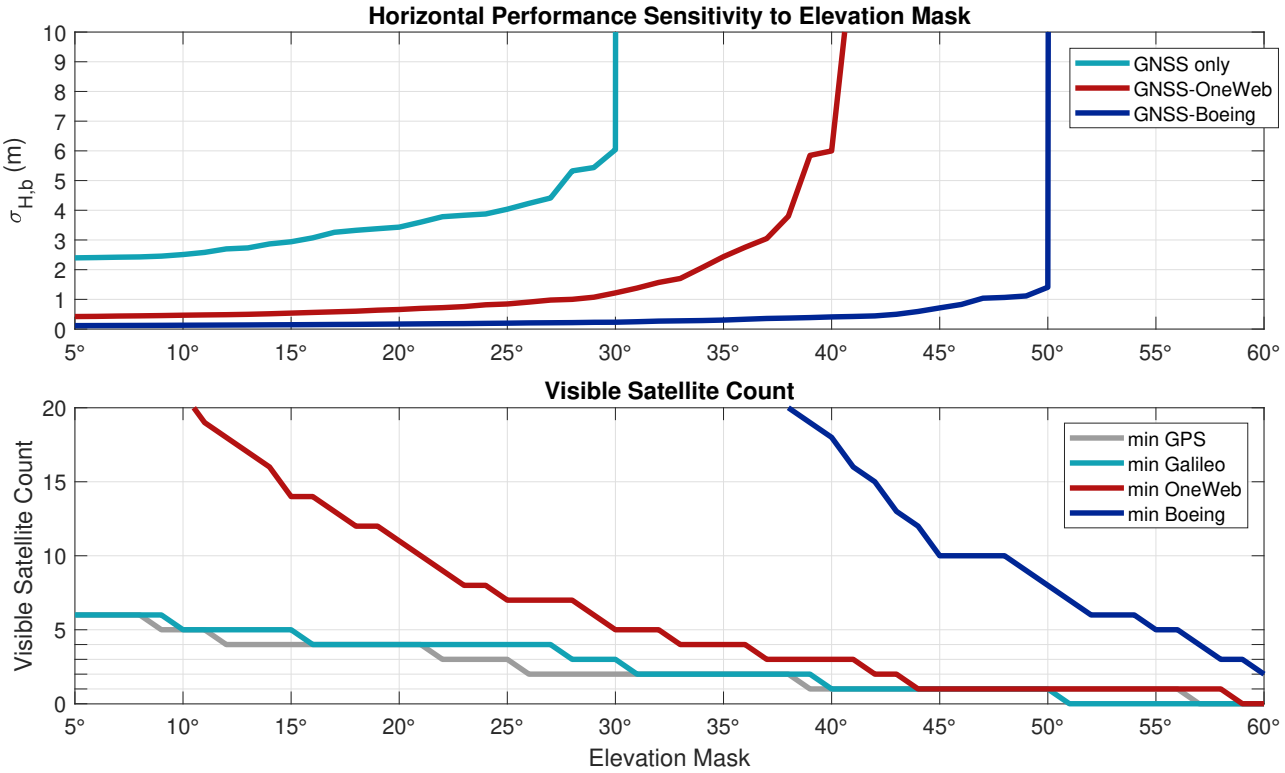

Figure 4: Elevation Sensitivity Performance Using GNSS Only in Tucson, Arizona. In the top plot, maximum horizontal positioning uncertainties over 24 hours are plotted for each elevation mask, for a user in Tucson, Arizona. The bottom plot shows the minimum number of visible satellites for each constellation over 24 hours for each elevation mask.

As the elevation mask increases, the number of visible satellites decreases, and $\sigma_{H,b}$ increases. Past 30°, the horizontal positioning error uncertainty can exceed 10m for GNSS only. With additional measurements from OneWeb, the bounding horizontal standard deviation stays under 6m up to an elevation mask of 40°. For the Boeing constellation, the bounding horizontal positioning uncertainty stays below 1.5m up to an elevation mask of 50°. In the next section, we assume an elevation mask of 40°.

4.2.2 Performance Sensitivity to Batch Period

The nominal case uses a 10-minute batch period. In this analysis, we look at the effect on positioning uncertainty of shortening and extending the batch period. We investigate the effect of using a batch period of 5 to 25 minutes at 5-minute intervals. All other simulation parameters are described in Section 4.1. The batch period sensitivity results using GNSS only, GNSS-OneWeb, and GNSS-Boeing are shown in Figure 5. We plot $\sigma_{H,b}$ values over 24 hours. We see the performance for $t_{\text{batch}} = 25\,\text{min}$ in dark blue, and the performance for $t_{\text{batch}} = 5\,\text{min}$ in dark red. The visible satellite count over 24 hours is shown on the bottom three plots of Figure 5.

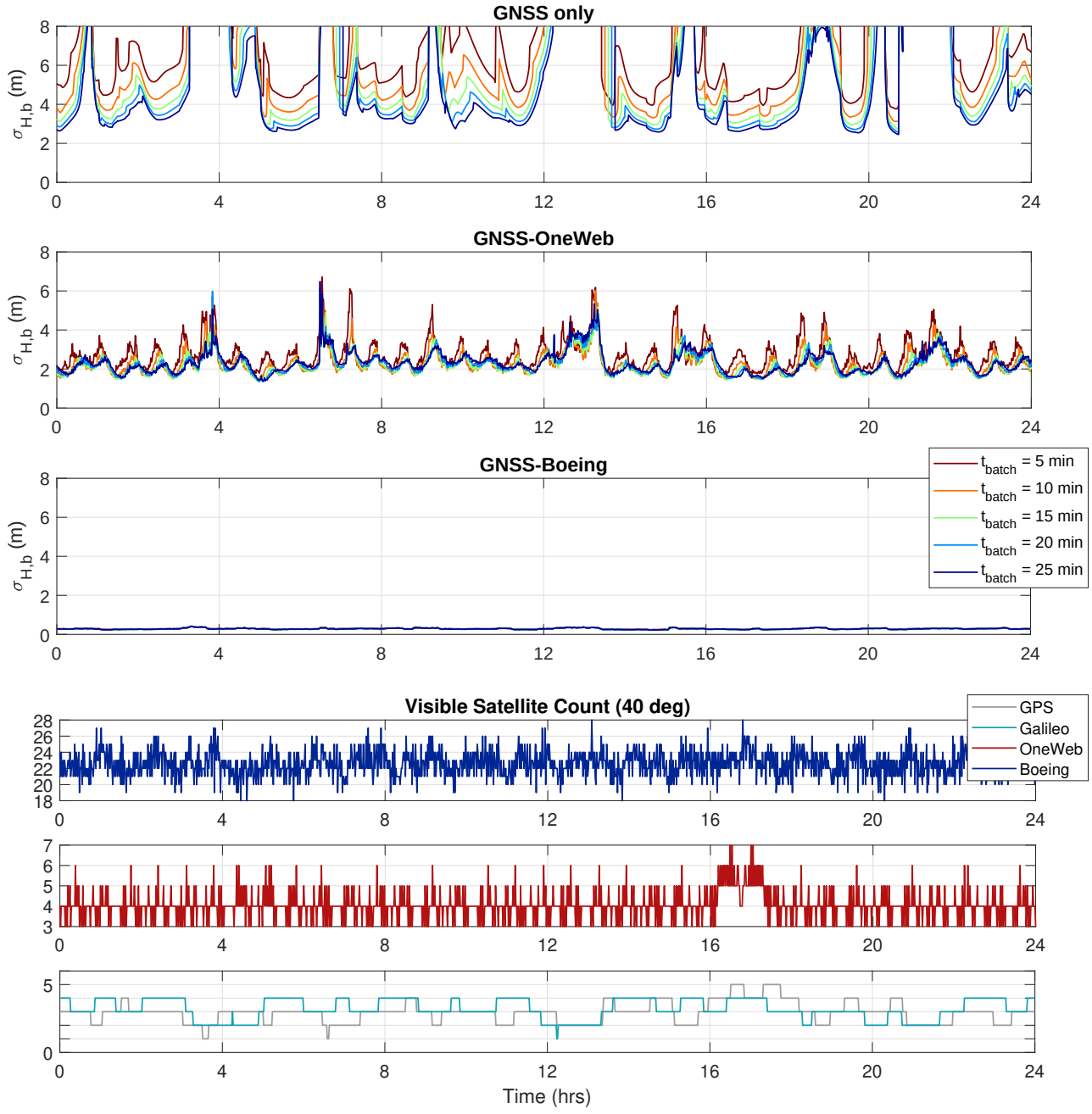

Figure 5: Batch Period Sensitivity Analysis Using a 40° Elevation Mask in Tucson, Arizona. The top three plots show the horizontal positioning performance over time using GNSS only, GNSS-OneWeb, and GNSS-Boeing for a range of batch periods. The bottom three plots show the number of visible satellites for GNSS, OneWeb, and Boeing over 24 hours, for a 40-degree elevation mask.

In the GNSS only case, increasing the batch period decreases $\sigma_{H,b}$ for time periods where the positioning uncertainty is under 8 meters. The spikes indicate a very large uncertainty in the horizontal user position. At these time periods where there are at most two GPS satellites or at most two Galileo satellites, GNSS measurements alone perform poorly for a 40-degree elevation mask. In the GNSS-OneWeb case, $\sigma_{H,b}$ stays under 7 meters, and we see two conflicting occurrences. On the one hand, the longer the batch period, the better the estimate because there are more measurements for noise averaging, and more satellite motion providing observability. On the other hand, the longer the batch period, the looser the variance bound using Langel's method. We find that if we narrow the $[T_{min}, T_{max}]$ range, i.e., if we tighten the positioning error bound, then only the former occurrence remains, and $\sigma_{H,b}$ values are lowest for $t_{\text{batch}} = 25$ minutes. In the GNSS-Boeing case, changing the batch period has little effect on the consistent sub-meter $\sigma_{H,b}$ values. We find that even for a batch period of 1 minute, $\sigma_{H,b}$ stays under 1 meter using GNSS-Boeing.

4.2.3 Performance Sensitivity to Measurement Sampling Rate

We look at the effect of taking measurements at measurement sampling intervals of 30, 60, 90, and 120 seconds for positioning using GNSS only, GNSS-OneWeb, and GNSS-Boeing. The results for all three configurations are shown in Figure 6.

Using GNSS only, changes in measurement sampling rate have little effect. This is caused by the fact that GNSS satellites have half-day orbital periods, and have very little apparent motion in the sky within the 10-minute batches. Taking measurements more frequently gives us "in-between" measurements that do not offer additional information.

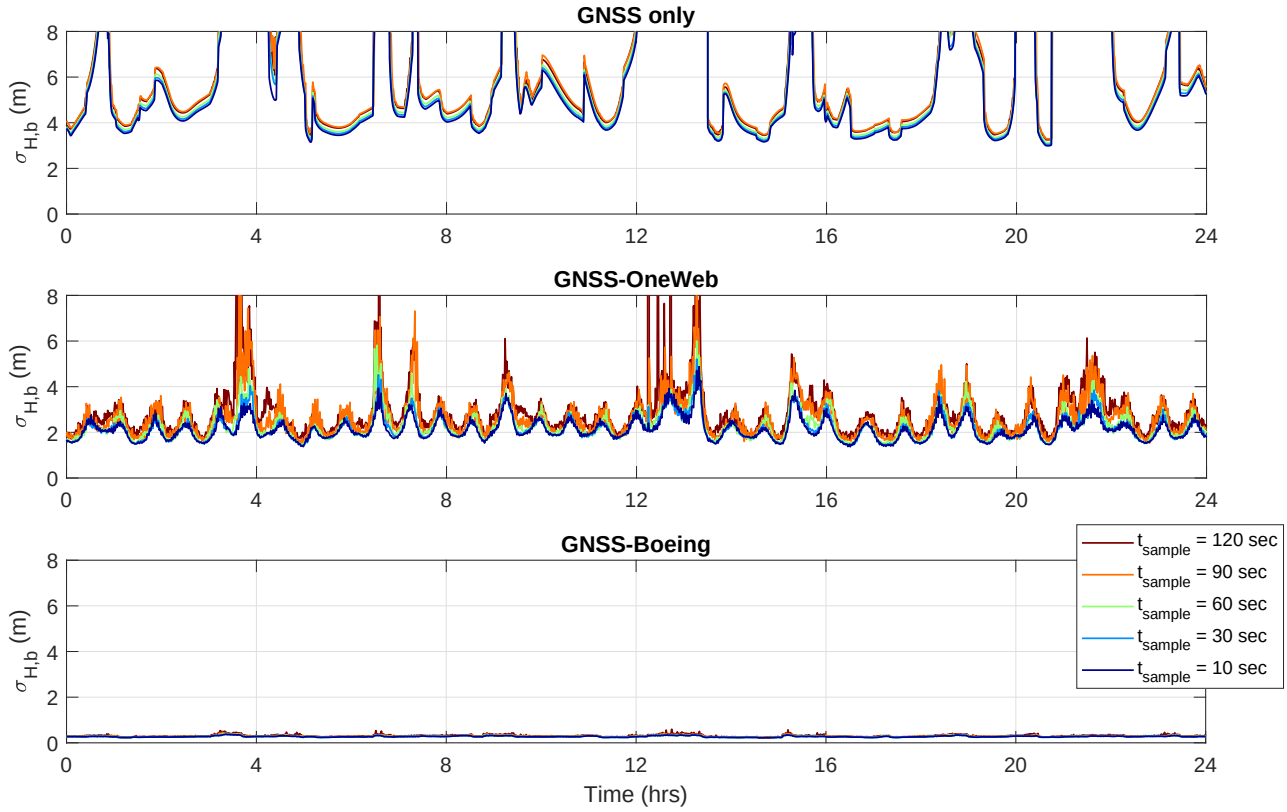

Figure 6: Measurement Sampling Rate Sensitivity Analysis Using a 40° Elevation Mask in Tucson, Arizona. The three plots show the horizontal positioning performance over time using GNSS only, GNSS-OneWeb, and GNSS-Boeing for a range of measurement sampling periods.

OneWeb satellites have an orbital period of about 100 minutes, and there is significant satellite motion provided by the OneWeb constellation within the 10-minute batch period. As a result, the horizontal positioning performance improves as the measurement sampling period gets smaller. Looking at the results for GNSS-Boeing on the third plot of Figure 6, we see that the different sampling rates have little effect to the consistent sub-meter horizontal positioning performance when using GNSS-Boeing.

4.2.4 Performance Sensitivity to Satellite Clock and Orbit Ephemeris Error

The ephemeris error is highly dependent on the orbit determination process, update rate, space weather, and density of ground monitoring stations. We look at the effect of the orbit determination process by varying the Gauss-Markov Process (GMP) standard deviation ($\sigma_{E,LEO}$) of the satellite ephemeris error model for the mega-constellations. We consider ephemeris error GMP standard deviation values of 0.015, 0.15, 1.5, 15, and 150 meters. We consider a large $\sigma_{E,LEO}$ value of 150 meters to see if we can match the performance using GNSS only, and investigate the margin of error tolerable for LEO satellite clock and orbit ephemeris. The results are plotted in Figure 7, which includes the results for GNSS only as a baseline (GNSS error parameters are kept nominal).

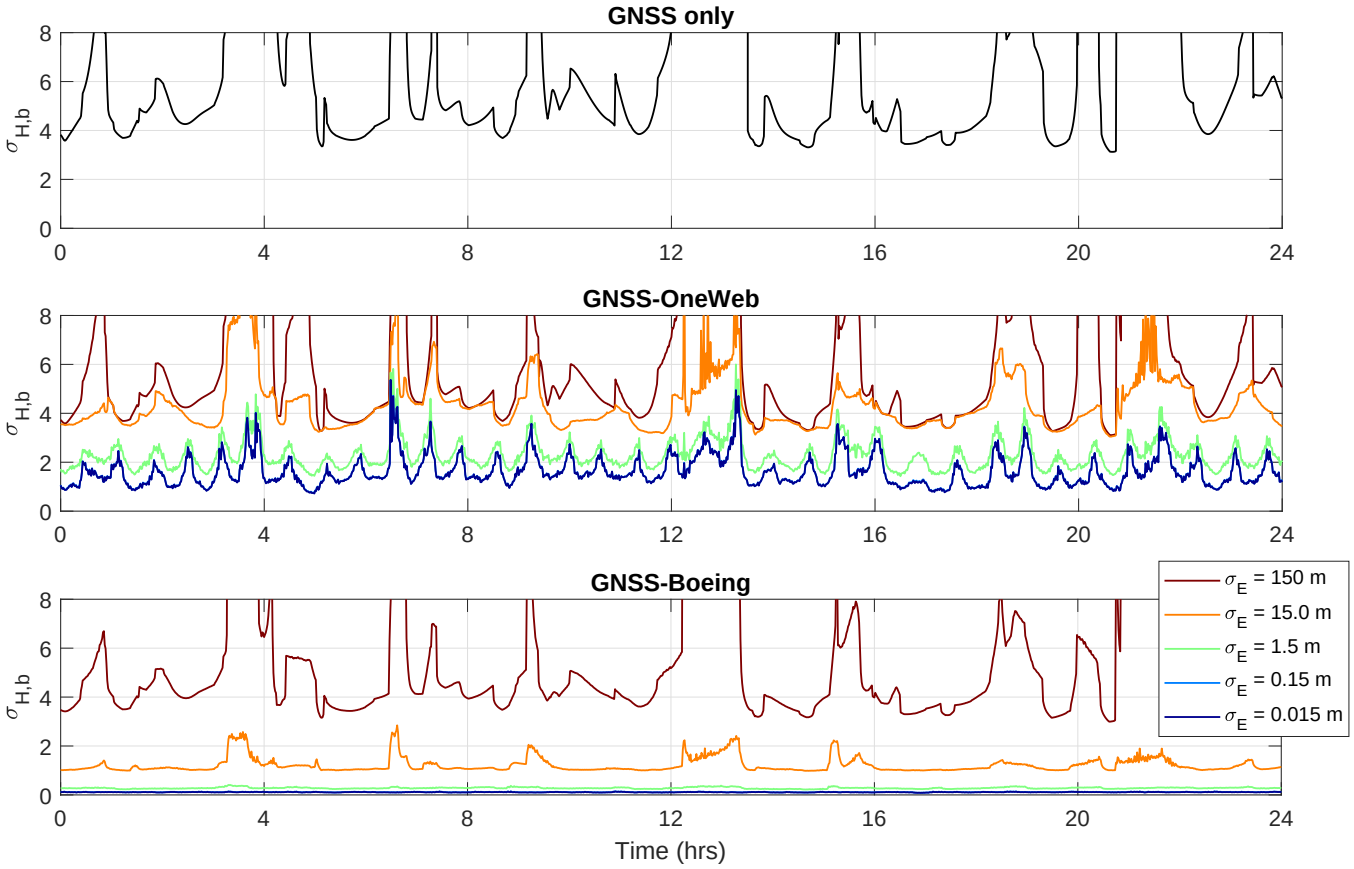

Figure 7: Ephemeris Error Sensitivity Analysis Using a 40° Elevation Mask in Tucson, Arizona. The plots show the horizontal positioning performance over time using GNSS only, GNSS-OneWeb, and GNSS-Boeing for a range of LEO ephemeris error GMP standard deviations.

In the GNSS-OneWeb case, the $\sigma_{H,b}$ plot for 0.015m and 0.15m are on top of each other, and provide the best horizontal positioning performance. At GMP standard deviation values of 15m and 150m, the horizontal positioning uncertainty using GNSS-OneWeb exceeds 5m for certain time periods. In the GNSS-Boeing case, the positioning performance stays well below 5 meters even at a GMP standard deviation of 15m.

4.3. Global Fault-Free Performance Analysis

In this section, we implement a covariance analysis for a grid of locations on Earth using nominal parameters (Section 4.1). This grid is created by dividing the globe into equally-spaced latitudes and longitudes at 10-degree intervals. At each grid point, we assess the fault-free availability using the criterion specified in Section 3.5. For this analysis, 10-minute batches are simulated at regular 10-minute intervals over 24 hours.

We implement separate fault-free availability analyses using GNSS only, GNSS-OneWeb, and GNSS-Boeing for a horizontal alert limit of 1.5 meters in two scenarios: (1) open sky with a 5-degree elevation mask, and (2) urban canyon with a 40-degree elevation mask. In Figures 8-10, the availability value is represented by colors that go from red (0% availability) to blue (100% availability).

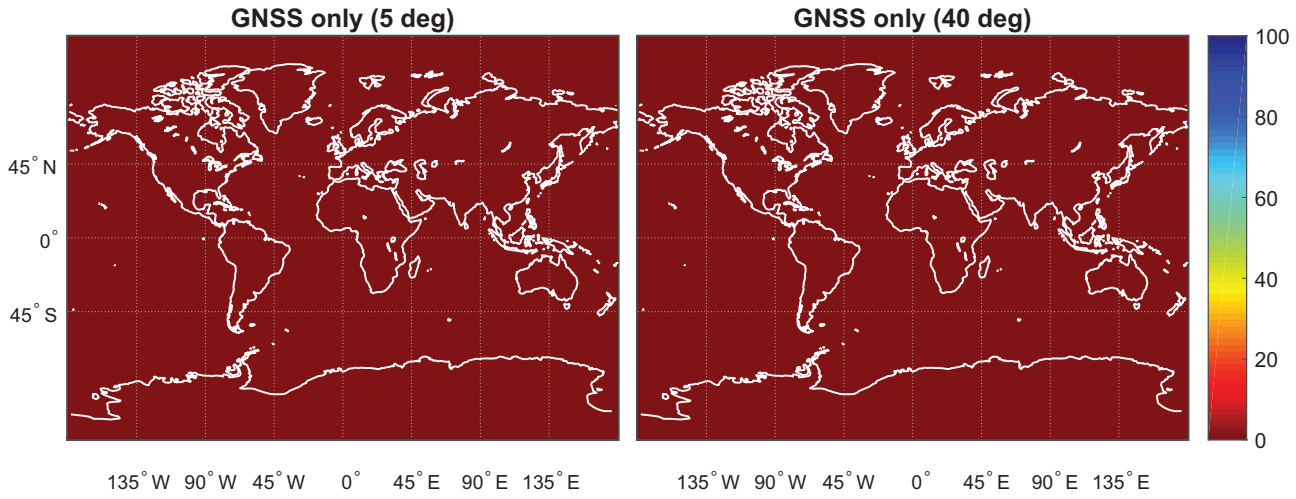

Figure 8: Fault-Free Availability Maps for 1.5m HAL using GNSS only. The availability maps show the horizontal positioning performance using GNSS only for open sky (left plot) and urban canyon (right plot) scenarios. Each grid point is assigned a color that represents the availability value at that location. The color bar on the right indicates the availability value for each color.

For this horizontal alert limit (HAL) of 1.5 meters, the GNSS only case provides 0% availability for both scenarios. In contrast, the availability map using GNSS-OneWeb for open sky scenario (left plot of Figure 9) shows 100% fault-free availability from mid to high latitudes (45 to 90° N-S), and fault-free availability values in the 90's range for the equatorial regions (0 to 45° N-S). This is because the distribution of satellites is denser at the poles and sparser in the equatorial region (see Figure 1). For a 5-degree elevation mask, GNSS-OneWeb provides 96.96% fault-free average availability for a horizontal alert limit of 1.5 meters in the 24-hour simulation period. Note that this value is the result of weighting each availability value by the cosine of latitude, which takes into account an ellipsoidal Earth where higher latitudes constitutes a smaller area of the map. We see great improvement from GNSS-only to GNSS-OneWeb for a 5-degree elevation mask, but do not quite achieve the same with the 40-degree elevation mask. To see a difference, we need to consider the GNSS-Boeing case.

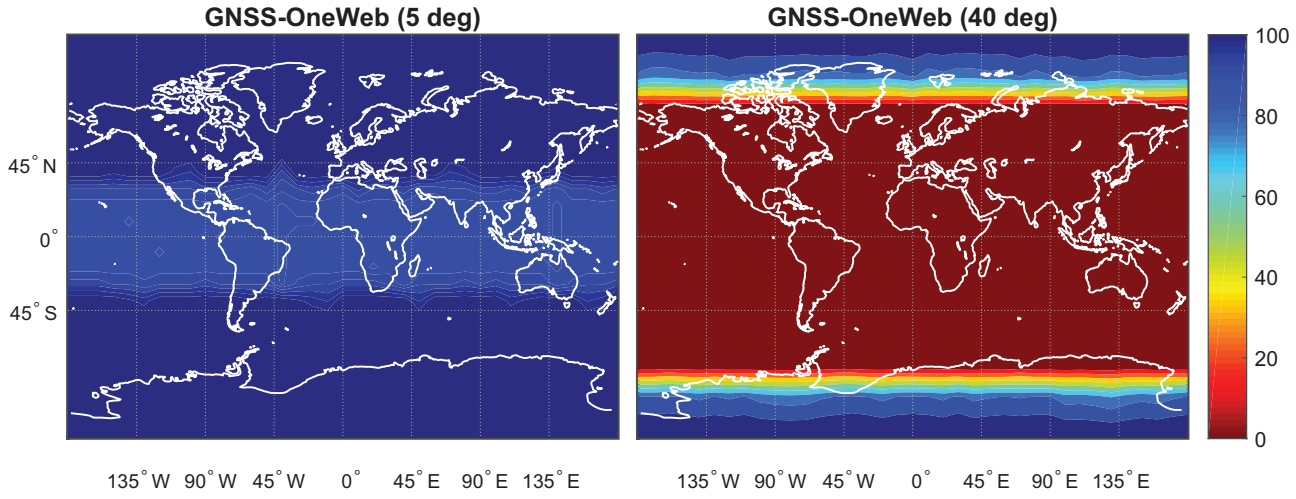

Figure 9: Fault-Free Availability Maps for 1.5m HAL using GNSS-OneWeb. The availability maps show the horizontal positioning performance using GNSS-OneWeb for open sky (left plot) and urban canyon (right plot) scenarios. Each grid point is assigned a color that represents the availability value at that location. The color bar on the right indicates the availability value for each color.

The open sky availability map using GNSS-Boeing (plot on the left of Figure 10) shows 100% fault-free average availability world-wide. The urban canyon availability map on the right of Figure 10 shows 85.63% fault-free average availability, and we see three different performance regions. The three sets of Boeing orbits results in red regions around 70°N-S, dark blue regions at low to mid-latitudes (20°-45°), and lighter blues in the equatorial region. This plot also shows that 100% FF availability in the continental US is achievable for a HAL value of 1.5 meters.

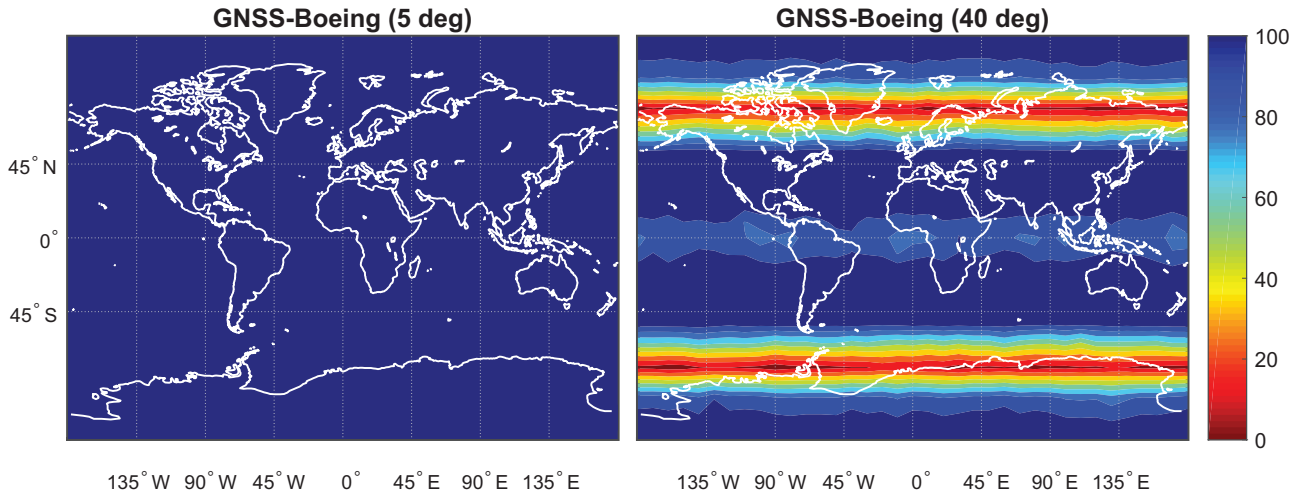

Figure 10: Fault-Free Availability Maps for 1.5m HAL using GNSS-Boeing. The availability maps show the horizontal positioning performance using GNSS-Boeing for open sky (left plot) and urban canyon (right plot) scenarios. Each grid point is assigned a color that represents the availability value at that location. The color bar on the right indicates the availability value for each color.

The table below shows the minimum values for HAL needed to achieve 100% worldwide fault-free availability using GNSS only, GNSS-OneWeb, and GNSS-Boeing, for open sky (5-degree elevation mask) scenarios. This table shows clearly the reduction in required HAL GNSS-MC can provide as compared to GNSS only.

Table 2: Minimum HAL Value to Achieve 100% Worldwide FF Availability

	GNSS only	GNSS-OneWeb	GNSS-Boeing
5 deg	11.37m	1.69m	0.58m

The horizontal alert limit of 1.5 meters was chosen as an example to highlight global trends when using either augmentation. A performance sensitivity analysis to varying values of HAL is given in [34] for a range of HAL values between 0.5 and 2 meters.

5. CONCLUSIONS

In this paper, we evaluated the horizontal positioning fault-free integrity performance achieved by a notional mega-constellation-augmented GNSS. We developed measurement error models for dual-frequency carrier phase measurements from LEO mega-constellations, and defined error model parameters for land vehicle applications. In this work, we derived a practical implementation of the method in [9] for upperbounding the positioning error variance to account for uncertainty in the error time correlation. An algorithm was derived for integrating dual-frequency measurements from GNSS with dual-frequency carrier phase measurements from LEO mega-constellations, which (1) leveraged satellite motion to estimate floating-valued cycle ambiguities and achieve rapid carrier phase positioning, and (2) accounted for time correlation in the errors. A sensitivity analysis was implemented for a single reference location, to evaluate the effect of varying elevation mask, batch period, measurement sampling rate, and satellite ephemeris error, on the positioning performance using GNSS only, GNSS-OneWeb, and GNSS-Boeing. We showed that for high elevation masks (>40 deg), longer batch periods have a significant impact on positioning performance when using GNSS-only and GNSS-OneWeb, but not so much on GNSS-Boeing. We also showed that measurement sampling within the batch has a smaller impact, which is desired for computational efficiency, and which also indicates that changes in satellite geometry are key to reducing estimation errors, more so than noise averaging. We implemented a worldwide fault-free availability analysis which revealed global trends in the horizontal positioning performance using GNSS-OneWeb and GNSS-Boeing, and showed promise of reducing the required horizontal alert limit for GNSS-MC as compared to GNSS-only.

APPENDIX

Matrices $\mathbf{V}_E$, $\mathbf{V}_T$, and $\mathbf{V}_M$ have similar structures. We use the notation $\mathbf{V}_\varepsilon$, where ε stands for E, T, M when designating ephemeris, tropospheric, and multipath respectively. Matrix $\mathbf{V}_\varepsilon$ is a block diagonal matrix that can be expressed as

$$\mathbf{V}_\varepsilon = \begin{bmatrix} {}^1\mathbf{V}_\varepsilon & \mathbf{0} & \dots & \mathbf{0} \\ \mathbf{0} & {}^2\mathbf{V}_\varepsilon & \ddots & \vdots \\ \vdots & \ddots & \ddots & \mathbf{0} \\ \mathbf{0} & \dots & \mathbf{0} & {}^n\mathbf{V}_\varepsilon \end{bmatrix}. \tag{33}$$

We express the non-zero diagonal block for satellite i as

$${}^i\mathbf{V}_\varepsilon = E\left\{ \begin{bmatrix} {}^i\mathscr{E}_{\varepsilon,1}\,{}^i\mathscr{E}_{\varepsilon,1} & \dots & {}^i\mathscr{E}_{\varepsilon,1}\,{}^i\mathscr{E}_{\varepsilon,q} \\ \vdots & \ddots & \vdots \\ {}^i\mathscr{E}_{\varepsilon,q}\,{}^i\mathscr{E}_{\varepsilon,1} & \dots & {}^i\mathscr{E}_{\varepsilon,q}\,{}^i\mathscr{E}_{\varepsilon,q} \end{bmatrix} \right\} \tag{34}$$

where the off-diagonal terms capture the error time-correlation. The error correlation terms between errors at time x and a later time y can be written as

$$E\left\{ {}^i\mathscr{E}_{\varepsilon,x}\,{}^i\mathscr{E}_{\varepsilon,y} \right\} = {}^ic_{\varepsilon,x}\,{}^ic_{\varepsilon,y}\,\sigma_\varepsilon^2\, e^{-\left(\frac{t_y - t_x}{T_\varepsilon}\right)} \tag{35}$$

where ${}^ic_\varepsilon$ is the elevation-dependent coefficient, σ_ε is the Gauss-Markov process (GMP) standard deviation, and T_ε is the GMP correlation time constant defined in Section 2.2. Given that the measurement sampling period $T_s = t_k - t_{k-1}$ is fixed, we define

$$\beta_\varepsilon = e^{-\left(\frac{T_s}{T_\varepsilon}\right)} \tag{36}$$

such that for satellite i, we can write the following:

$$\begin{array}{rcccl} E\left\{ {}^i\mathscr{E}_{\varepsilon,1}\,{}^i\mathscr{E}_{\varepsilon,1} \right\} & = & {}^ic_{\varepsilon,1}^2\,\beta_\varepsilon^0\,\sigma_\varepsilon^2 & = & {}^ic_{\varepsilon,1}^2\,\sigma_\varepsilon^2 \\ E\left\{ {}^i\mathscr{E}_{\varepsilon,1}\,{}^i\mathscr{E}_{\varepsilon,2} \right\} & = & {}^ic_{\varepsilon,1}\,{}^ic_{\varepsilon,2}\,\beta_\varepsilon^1\,\sigma_\varepsilon^2 & = & E\left\{ {}^i\mathscr{E}_{\varepsilon,2}\,{}^i\mathscr{E}_{\varepsilon,1} \right\} \\ E\left\{ {}^i\mathscr{E}_{\varepsilon,1}\,{}^i\mathscr{E}_{\varepsilon,3} \right\} & = & {}^ic_{\varepsilon,1}\,{}^ic_{\varepsilon,3}\,\beta_\varepsilon^2\,\sigma_\varepsilon^2 & = & E\left\{ {}^i\mathscr{E}_{\varepsilon,3}\,{}^i\mathscr{E}_{\varepsilon,1} \right\} \\ \vdots & & \vdots & & \vdots \\ E\left\{ {}^i\mathscr{E}_{\varepsilon,1}\,{}^i\mathscr{E}_{\varepsilon,q} \right\} & = & {}^ic_{\varepsilon,1}\,{}^ic_{\varepsilon,q}\,\beta_\varepsilon^{q-1}\,\sigma_\varepsilon^2 & = & E\left\{ {}^i\mathscr{E}_{\varepsilon,q}\,{}^i\mathscr{E}_{\varepsilon,1} \right\}. \end{array}$$

Equation (34) can then be written as

$${}^i\mathbf{V}_\varepsilon = {}^i\begin{bmatrix} c_1^2\sigma^2 & c_1c_2\beta\sigma^2 & c_1c_3\beta^2\sigma^2 & \dots & c_1c_q\beta^{q-1}\sigma^2 \\ c_1c_2\beta\sigma^2 & c_2^2\sigma^2 & c_2c_3\beta\sigma^2 & & \\ c_1c_3\beta^2\sigma^2 & c_2c_3\beta\sigma^2 & c_3^2\sigma^2 & & \vdots \\ \vdots & & & \ddots & \\ c_1c_q\beta^{q-1}\sigma^2 & & \dots & & c_q^2\sigma^2 \end{bmatrix}_\varepsilon \tag{37}$$

where the left superscript i, and right subscript ε are placed outside the matrix for clarity of presentation. For algorithm coding convenience, equation (37) is written as

$${}^i\mathbf{V}_\varepsilon = \sigma_\varepsilon^2\,{}^i\begin{bmatrix} c_1^2 & c_1c_2 & c_1c_3 & \dots & c_1c_q \\ c_1c_2 & c_2^2 & c_2c_3 & & \\ c_1c_3 & c_2c_3 & c_3^2 & & \vdots \\ \vdots & & & \ddots & \\ c_1c_q & & \dots & & c_q^2 \end{bmatrix}_\varepsilon \circ \begin{bmatrix} \beta^0 & \beta^1 & \beta^2 & \dots & \beta^{q-1} \\ \beta^1 & \beta^0 & \beta^1 & & \\ \beta^2 & \beta^1 & \beta^0 & & \vdots \\ \vdots & & & \ddots & \\ \beta^{q-1} & & \dots & & \beta^0 \end{bmatrix}_\varepsilon \tag{38}$$

where "∘" indicates element-by-element multiplication of matrices. We make the following definitions

$$
{}^{i}\mathbf{c}_{\varepsilon} = {}^{i}\begin{bmatrix} c_1 \\ c_2 \\ c_3 \\ \vdots \\ c_q \end{bmatrix}_{\varepsilon} \qquad \mathbf{B} = \begin{bmatrix} 0 & 1 & 2 & \dots & q-1 \\ 1 & 0 & 1 & & \\ 2 & 1 & 0 & & \vdots \\ \vdots & & & \ddots & \\ q-1 & & \dots & & 0 \end{bmatrix} \tag{39}
$$

where ${}^{i}\mathbf{c}_{\varepsilon}$ is the vector of elevation-dependent coefficients stacked at all times for satellite i, for error source ε. These definitions result in the following compact expression

$$
{}^{i}\mathbf{V}_{\varepsilon} = \sigma_{\varepsilon}^{2}\, {}^{i}\mathbf{c}_{\varepsilon}\, {}^{i}\mathbf{c}_{\varepsilon}^{\mathrm{T}} \circ \exp \circ \left(-\frac{T_s}{T_{\varepsilon}} \mathbf{B} \right) \tag{40}
$$

where "exp ∘" represents the element-wise exponential function applied to matrix $\left(-\frac{T_s}{T_{\varepsilon}}\mathbf{B}\right)$. We can now specify expressions for covariance matrices ${}^{i}\mathbf{V}_{E}$, ${}^{i}\mathbf{V}_{T}$, and ${}^{i}\mathbf{V}_{M}$. The expression for ${}^{i}\mathbf{V}_{R}$ is also included for completeness.

$$
\begin{aligned}
{}^{i}\mathbf{V}_{E} &= \sigma_{E}^{2} \exp\left(-\frac{T_s}{T_E} \mathbf{B} \right) \\
{}^{i}\mathbf{V}_{T} &= \sigma_{T}^{2}\, {}^{i}\mathbf{c}_{T}\, {}^{i}\mathbf{c}_{T}^{\mathrm{T}} \circ \exp\left(-\frac{T_s}{T_T} \mathbf{B} \right) \\
{}^{i}\mathbf{V}_{M} &= \sigma_{M}^{2}\, {}^{i}\mathbf{c}_{M}\, {}^{i}\mathbf{c}_{M}^{\mathrm{T}} \circ \exp\left(-\frac{T_s}{T_M} \mathbf{B} \right) \\
{}^{i}\mathbf{V}_{R} &= \begin{bmatrix} {}^{i}\sigma_{R,1}^{2} & 0 & \dots & 0 \\ 0 & {}^{i}\sigma_{R,2}^{2} & \ddots & \vdots \\ \vdots & \ddots & \ddots & 0 \\ 0 & \dots & 0 & {}^{i}\sigma_{R,q}^{2} \end{bmatrix}
\end{aligned} \tag{41}
$$

References

[1] P. Misra and P. Enge, *Global Positioning System: Signals, Measurements, and Performance*. Lincoln, Massachusetts: Ganga-Jamuna Press, revised se ed., 2012.

[2] R. J. Danchik, "An Overview of Transit Development," *Johns Hopkins APL Technical Digest (Applied Physics Laboratory)*, vol. 19, no. 1, pp. 18–26, 1998.

[3] M. Rabinowitz, *A Differential Carrier-Phase Navigation System Combining GPS with Low Earth Orbit Satellites for Rapid Resolution of Integer Cycle Ambiguities*. PhD thesis, Stanford University, 2001.

[4] M. Joerger, J. Neale, B. Pervan, and S. Datta-Barua, "Measurement Error Models and Fault-Detection Algorithms for Multi-Constellation Navigation Systems," in *IEEE/ION Position, Location and Navigation Symposium*, pp. 927–946, 2010.

[5] C. T. Ardito, J. J. Morales, J. J. Khalife, A. A. Abdallah, and Z. M. Kassas, "Performance Evaluation of Navigation Using LEO Satellite Signals with Periodically Transmitted Satellite Positions," pp. 306–318, 2016.

[6] T. G. Reid, A. M. Neish, T. Walter, and P. K. Enge, "Broadband LEO Constellations for Navigation," *Navigation, Journal of the Institute of Navigation*, vol. 65, no. 2, pp. 205–220, 2018.

[7] J. Lee, Y. T. Morton, J. Lee, H. S. Moon, and J. Seo, "Monitoring and Mitigation of Ionospheric Anomalies for GNSS-Based Safety Critical Systems: A review of up-to-date signal processing techniques," *IEEE Signal Processing Magazine*, vol. 34, no. 5, pp. 96–110, 2017.

[8] M. Joerger, J. Neale, S. Datta-Barua, and B. Pervan, "Ionospheric error modeling for carrier phase-based multiconstellation navigation systems," *IEEE Transactions on Aerospace and Electronic Systems*, vol. 49, no. 1, pp. 451–467, 2013.

[9] S. E. Langel, *Bounding Estimation Integrity Risk for Linear Systems with Structured Stochastic Modeling Uncertainty*. PhD thesis, Illinois Institute of Technology, 2014.

[10] Radio Technical Commission for Aeronautics (RTCA) Special Committee 159, "Minimum Operational Performance Standards for Global Positioning System/Wide Area Augmentation System Airborne Equipment," 2009.

[11] C. Henry, "OneWeb Shifts First Launch to Year's End." `https://spacenews.com/oneweb-shifts-first-launch-to-years-end/`, May 2018. (Accessed on 06/27/2019).

[12] R. J. Barnett, "OneWeb Non-Geostationary Satellite System: Technical Information to Supplement Schedule S," 2016.

[13] A. Nyirady, "OneWeb Successfully Launches 1st Batch of Satellites." `https://www.satellitetoday.com/launch/2019/02/28/oneweb-successfully-launches-1st-batch-of-satellites/`, February 2019. (Accessed on 06/27/2019).

[14] C. Henry, "Boeing Constellation Stalled, SpaceX Constellation Progressing." `https://spacenews.com/boeing-constellation-stalled-spacex-constellation-progressing/`, June 2018. (Accessed on 06/27/2019).

[15] P. B. de Selding, "Boeing Proposes Big Satellite Constellations in V- and C-bands." `https://spacenews.com/boeing-proposes-big-satellite-constellations-in-v-and-c-bands/`, June 2016. (Accessed on 06/27/2019).

[16] W. A. Hanson, "In Their Own Words, OneWeb Internet Constellation as Described in their FCC From 312 Application," 2016.

[17] T. Azzarelli, "OneWeb: Access for Everyone," in *ITU International Satellite Symposium*, 2016.

[18] T. Walter, J. Blanch, and P. Enge, "Evaluation of Signal in Space Error Bounds to Support Aviation Integrity," *NAVIGATION, Journal of the Institute of navigation)*, vol. 57, no. 2, pp. 101–113, Summer 2010.

[19] T. Walter and J. Blanch, "KEYNOTE - Characterization of GNSS Clock and Ephemeris Errors to Support ARAIM," in *Proceedings of the ION 2015 Pacific PNT Meeting*, (Honolulu, Hawaii), pp. 920–931, April 2015.

[20] T. Walter, K. Gunning, R. Eric Phelts, and J. Blanch, "Validation of the Unfaulted Error Bounds for ARAIM," *Navigation: Journal of The Institute of Navigation*, vol. 65, no. 1, pp. 117–133, 2018.

[21] Working Group C, "EU-US Cooperation on Satellite Navigation Working Group C, ARAIM Technical Subgroup, Milestone 3 Report," no. 1, pp. 1–76, 2016.

[22] Radio Technical Commission for Aeronautics (RTCA) Special Committee 159, "Minimum Operational Performance Standards for Global Positioning System/Wide Area Augmentation System Airborne Equipment," 2006.

[23] S. Khanafseh, B. Kujur, M. Joerger, T. Walter, S. Pullen, J. Blanch, K. Doherty, L. Norman, L. de Groot, and B. Pervan, "GNSS Multipath Error Modeling for Automotive Applications," *Proceedings of the 31st International Technical Meeting of The Satellite Division of the Institute of Navigation (ION GNSS+ 2018)*, pp. 1573–1589, 2018.

[24] M. Joerger, *Carrier Phase GPS Augmentation Using Laser Scanners and Using Low Earth Orbiting Satellites*. PhD thesis, Illinois Institute of Technology, 2009.

[25] M. Joerger, J. Neale, and B. Pervan, "Iridium/GPS Carrier Phase Positioning and Fault Detection Over Wide Areas," *22nd International Technical Meeting of the Satellite Division of the Institute of Navigation 2009, ION GNSS 2009 Volume 3, 2009, Pages 1685-1699*, vol. 3, no. November, pp. 1685–1699, 2009.

[26] M. Joerger and B. Pervan, "Multi - Constellation ARAIM Exploiting Satellite Motion," unpublished.

[27] M. Joerger and B. Pervan, "Exploiting Satellite Motion in ARAIM: Measurement Error Model Refinement Using Experimental Data," in *Proceedings of the 29th International Technical Meeting of The Satellite Division of the Institute of Navigation (ION GNSS+ 2016)*, 2016.

[28] M. Joerger, S. Stevanovic, F.-C. Chan, S. Langel, and B. Pervan, "Integrity Risk and Continuity Risk for Fault Detection and Exclusion Using Solution Separation ARAIM," in *Proceedings of the 26th International Technical Meeting of The Satellite Division of the Institute of Navigation (ION GNSS 2013)*, 2013.

[29] B. Pervan, *Navigation Integrity for Aircraft Precision Landing Using the GPS*. PhD thesis, Stanford University, 1996.

[30] S. Langel, O. Garcia Crespillo, and M. Joerger, "Bounding Sequential Estimation Errors Due to Gauss-Markov Noise with Uncertain Time Constants," in *Proceedings of the ION GNSS+ 2019*, (Miami, Florida), September 2019.

[31] E. Gallon, M. Joerger, S. Perea, and B. Pervan, "Error Model Development for ARAIM Exploiting Satellite Motion," in *Proceedings of the ION GNSS+ 2019*, (Miami, Florida), September 2019.

[32] B. Pervan, S. Khanafseh, and J. Patel, "Test Statistic Auto- and Cross-correlation Effects on Monitor False Alert and Missed Detection Probabilities," in *Proceedings of the 2017 International Technical Meeting of The Institute of Navigation*, (Monterey, California), pp. 562–590, January 2017.

[33] J. Haase, M. Ge, H. Vedel, and E. Calais, "Accuracy and Variability of GPS Tropospheric Delay Measurements of Water Vapor in the Western Mediterranean," *Journal of Applied Meteorology)*, vol. 42, pp. 1547–1568, November 2003.

[34] D. Racelis, "Fault-Free Integrity Analysis of Mega-Constellation-Augmented GNSS," Master's thesis, University of Arizona, 2019.